Received: 7 February 2023 | Revised: 11 December 2023 | Accepted: 5 January 2024

DOI: 10.1111/micc.12845

Microcirculation WILEY

ORIGINAL ARTICLE

Impact of stalling events on microcirculatory hemodynamics in the aged brain

Mohammad Jamshidi[1] | Thomas Ventimiglia[1] | Patrice Sudres[1] | Cong Zhang[2] | Frédéric Lesage[2] | William Rooney[3] | Daniel Schwartz[3] | Andreas A. Linninger[1,4]

[1]Department of Biomedical Engineering, University of Illinois at Chicago, Chicago, Illinois, USA

[2]Department of Electrical Engineering, Polytechnique Montréal, Montreal, Canada

[3]Advanced Imaging Research Center, Oregon Health & Science University, Portland, Oregon, USA

[4]Department of Neurosurgery, University of Illinois at Chicago, Chicago, Illinois, USA

Correspondence
Andreas A. Linninger, Department of Biomedical Engineering, University of Illinois at Chicago, Chicago, Illinois, USA.
Email: linninge@uic.edu

Abstract

Objective: The role of cerebral microvasculature in cognitive dysfunction can be investigated by identifying the impact of blood flow on cortical tissue oxygenation. In this paper, the impact of capillary stalls on microcirculatory characteristics such as flow and hematocrit (Ht) in the cortical angioarchitecture is studied.

Methods: Using a deterministic mathematical model to simulate blood flow in a realistic mouse cortex, hemodynamics parameters, including pressure, flow, vessel diameter-adjustable hematocrit, and transit time are calculated as a function of stalling events.

Results: Using a non-linear plasma skimming model, it is observed that Ht increases in the penetrating arteries from the pial vessels as a function of cortical depth. The incidence of stalling on Ht distribution along the blood network vessels shows reduction of RBCs around the tissue near occlusion sites and decreased Ht concentration downstream from the blockage points. Moreover, upstream of the occlusion, there is a noticeable increase of the Ht, leading to larger flow resistance due to higher blood viscosity. We predicted marked changes in transit time behavior due to stalls which match trends observed in mice in vivo.

Conclusions: These changes to blood cell quantity and quality may be implicated in the development of Alzheimer's disease and contribute to the course of the illness.

KEYWORDS
capillary stalling, cerebral blood flow, cerebral hemodynamics, mathematical modeling, microcirculation

1 | INTRODUCTION

The cerebral vascular network plays an important role in ensuring oxygen exchange and blood perfusion to the brain. Modulation of hemodynamic aspects of this vascular space is necessary to respond to metabolic need to maintain homeostasis and is achieved by an interaction between neurons, blood vessels and other extracellular factors, collectively named the neurovascular unit (NVU)[1,2]. Disruption to this coupling may significantly impact cognitive capacity; it is thought that significant disruption to these mechanisms may

Abbreviations: CBF, cerebral blood flow; Hd, discharge hematocrit; Ht, hematocrit; KPSM, kinematic plasma skimming model; NVU, neurovascular unit; NWK, network; RBC, red blood cell.

occur in aging and be more pronounced in both chronic and acute late-life neurological disease.[3–5] One of the top 10 leading causes of mortality globally, notably in the United States, is cognitive illnesses such as dementia, including Alzheimer's disease.[6] By 2060, the number of persons in the United States with Alzheimer's disease is anticipated to triple.[7] These statistics demonstrate the importance of research studies in developing more efficient, affordable, and accessible treatment methods.[8] Current clinical neuroimaging approaches lack the resolution to measure all pertinent aspects of the NVU, and available diagnostic methods often do not have the sensitivity for signs in prodromal stages of disease when therapy is most effective. A model-based simulation approach that allows for inference of pathological changes at a scale unavailable to in vivo examination in the clinic would provide detection and diagnosis of age-related diseases at earlier stages.[3] A mechanistic model capable of accurately simulating complex dynamic relationships in the NVU may also elucidate the role of cerebral microvasculature in healthy aging and cognitive decline by identifying factors with the potential to produce significant disruption to perfusion in vascular networks at multiple scales.[9]

A recent comprehensive study used deterministic hemodynamic modeling to predict the effect of stalling on microcirculatory blood flow and investigated the correlation between the stall ratios and cerebral blood flow.[10] Here, we posit that in addition to flow changes, changes in hematocrit distribution especially in microvessels may impair cognitive function. Even with intact plasma perfusion, oxygen transfer may still be poor owing to an uneven distribution of the hematocrit. Lower hematocrit fluxes may impair oxygen transfer to the target tissues either upstream or downstream of the occluded vessels.

Most prior research focused on the obstruction of primary penetrating arteries often referred to as the "perfusion bottleneck".[11,12] Other studies considered the flow changes after single capillary vessel occlusion and evaluated its local effect on blood flow.[13] In recent studies, the presence of capillary stalls was implicated as a substantial contributor to insufficient post-stroke reperfusion.[14,15] This led to several studies investigating the incidence of capillary occlusion in different tissues under different conditions. For example, one study using intravital microscopy found that capillary occlusion occurred in around 5% of capillaries in the cremaster muscle of mice during ischemia–reperfusion injury.[16] Another study found that the incidence of capillary occlusion in the retina of rats increased from around 1% under normal conditions to around 10% during hyperoxia.[17] Recent computational efforts to address the relationship between the NVU and vascular hemodynamics[18–20] have suffered from vascular network simplifications, including using small synthetic networks, and arbitrary vessel diameter, though these simplifications are an inevitable part of models limited by computing power, modern neurovascular images which suffer from the capturing the high-quality image resolution and limited line-of-vision an essential division of the cortical microstructures.

Here we hypothesize that capillary stalls that diminish blood flow may leave a fingerprint in the transit time behavior of the entire blood flow network. The exploration of this idea is significant because it would inform in vivo imaging methods about avenues toward detecting the presence and perhaps even the extent of capillary occlusions that cannot be directly observed; an important step towards biomarkers of capillary dysfunction. We propose to use mechanistic hemodynamic simulation in realistic microvascular network graphs to systematically quantify the effect of stalling on perfusion and distribution of red blood cells (hematocrit). We perform mechanistic simulations for microcirculatory blood vessel networks extracted from the mouse somatosensory cortex including all ranges of vessels from large branches on the cortical surface to penetrating arteries, capillaries, and ascending veins.[11]

Since there is a direct relationship between blood flow and the oxygenation of microvascular networks,[21] one of the essential factors in estimating oxygen levels is to calculate the hematocrit (Ht) distribution in the vascular network, particularly in the capillary bed. To assess the impact of microstrokes on oxygenation, we apply a mechanistic hemodynamic model that can predict the red blood cell (RBC) distribution and hematocrit (Ht) split at each bifurcation, where hematocrit indicates the fraction of red blood cells to total blood volume (plasma and RBCs).[22,23] Blood flow properties such as flow, pressure, Ht, and transit time in the mouse brain cortex with and without capillary obstructions for healthy and capillary obstruction situations are computed locally and globally. We hypothesize that in cases of occlusion, a change in Ht is an additional factor for reduced oxygen in corresponding vessels in addition to decreases in local blood flow.

2 | MATHEMATICAL METHOD

2.1 | Governing equations

The blood in the network is considered as a suspension of blood plasma and red blood cells (RBCs). The Hagen–Poiseuille law is used in the network for flow continuity, estimating the bulk flow by connecting the volumetric flow to the pressure gradient at each vessel as a function of the diameter and hematocrit-dependent resistance. $\alpha, L, d, H_d, \mu_{vM}$ are hydraulic resistance, length of a vessel, vessel diameter, hematocrit, and modified in-vitro viscosity,[24] respectively.

Since blood viscosity in micro vessels is shear (diameter) and hematocrit dependent, a hematocrit-dependent viscosity law and a procedure for predicting uneven red blood cell splitting (plasma skimming) law is needed.

$$\alpha f = \nabla p \tag{1}$$

$$\vec{\nabla} \cdot f = 0 \tag{2}$$

$$\alpha = \frac{128L}{\pi d^4} \mu_{vM}(d, H_d) \tag{3}$$

$$\begin{bmatrix} A(h,d) & -C_1 \\ (1-D)C_1^T & D \end{bmatrix} \begin{bmatrix} f \\ p \end{bmatrix} = \begin{bmatrix} 0 \\ D\bar{p} \end{bmatrix} \tag{4}$$

2.2 | Non-linear viscosity

Lipowsky et al.[25] proposed a model for the apparent viscosity as a function of vessel diameter and hematocrit. Pries offered an alternative parametric description of blood viscosity termed the "in-vitro modified" formula.[26,27] His model predicts that the apparent viscosity decreases with decreasing diameters until $d=40\,\mu m$, below this level viscosity rises again with decreasing diameter. The viscosity model, given in Appendix A, is a function of the hematocrit and diameter (A-1). The relative apparent blood viscosity for a fixed discharge hematocrit H_d of 0.45 (or 45%), $\mu^*_{0.45}$ is given by (A-2), where D is the lumen diameter of the tube. The viscosity dependence on hematocrit is applied by the parameter C given by (A-3), μ_{plasma} is plasma viscosity equal to 0.001 cP.

The complete blood pressure and flow in matrix form[28] is given in Equation 4., where $A(h,d)$ is the resistance matrix dependent on the hematocrit and the vessel diameters, C_1 is the connectivity matrix that shows the point's connections relations in the network, p is the pressure, and $\bar{p}$ is the Dirichlet boundary condition for pressure. The binary matrix D encodes the boundary conditions at the outlet nodes: it is an $n_p \times n_p$ diagonal matrix whose value in the (i, i) position is nonzero if i is an outflow node and whose value is $-f_i$, where f_i is the volumetric flow in the adjacent face.[28] The system needs to be solved iteratively, because the hematocrit distribution, h, is initially not known.

2.3 | Prediction of the hematocrit field as a convection problem

We showed previously[24] that several prior formulations of plasma skimming predictions do not converge. As a remedy, we proposed a kinematic plasma skimming model (KPSM) that always converges. Moreover, we will show that by assigning an adjusted hematocrit potential H^* at each node, the hematocrit fields can be computed as a stationary convection problem, which is guaranteed to have a solution in acyclic network graphs.[3]

We model plasma skimming leading to a downstream hematocrit change, $\Delta H = H_1 - H_2$ by rewriting the red blood cell balance in terms of an adjusted discharge hematocrit, H^*, and a kinematic plasma-skimming coefficient, θ, as indicated in Equation 5. The discharge hematocrit into the side branches is calculated by enforcing the RBC split balance in Equation 6.[24] These terms indicate hematocrit depletion, and this solution process is illustrated in Figure 1.

$$H_2 = H_1 - \Delta H = \theta_2 . H^*, H_3 = \theta_3 . H^* \tag{5}$$

$$fH_1 = f_2 H_2 + f_3 H_3 = f_2 \theta_2 H^* + f_3 \theta_3 H^* \tag{6}$$

$$fH_1 = \hat{f}_2 H^* + \hat{f}_3 H^* \tag{7}$$

The full hematocrit (Ht) matrix equation for the steady RBC transport through a blood network is given in Equation 9 and

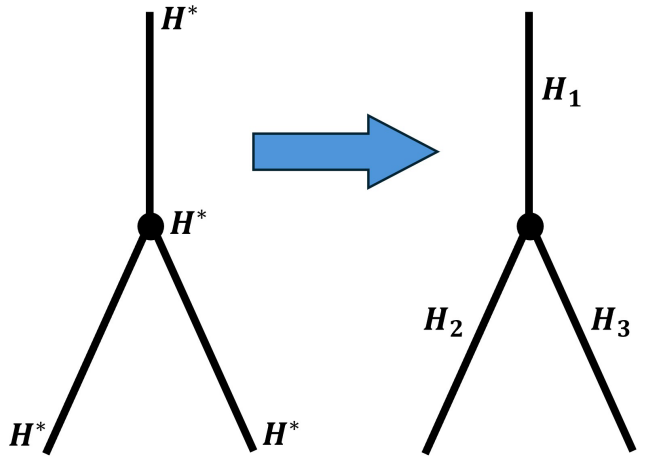

FIGURE 1 Recovery of the face hematocrit from nodalH^*.

introduced in.[4] The system can be interpreted as a convection problem in which the desired hematocrit values for each face are calculated by transporting nodal H* values through the network using flow rates that are adjusted by the kinematic plasma skimming coefficient. The effect is that thicker branches with more flow tend to have higher hematocrit compared to the side branches.

$$\hat{f} \cdot \vec{\nabla} H^* = 0 \tag{8}$$

$$M_c H^* + Q_o H^* + Q_i \overline{H} = 0 \tag{9}$$

$$\hat{f} = f_i \theta_i \tag{10}$$

$$\theta_i = \left(\frac{d_i}{d_p} \right)^{\frac{2}{m}} \tag{11}$$

In the system defined by Equations (7)–(10), the vector $\hat{f}$ in R^{n_f}, represents the adjusted flow rates, calculated as the product of blood flows at each segment and the skimming coefficient θ. The coefficient vector θ in R^{n_f} is associated with the kinematic plasma-skimming at bifurcations. It is determined by the diameter ratio $\left(\frac{d_i}{d_p} \right)$ and scalar drift parameter $m=5.25$.[3] The convection matrix M_c given by $-C_1^T \max\left(\text{diag}\, \hat{f} * C_1, 0 \right)$, Here $\hat{f} \in R^{n_f}$ is a vector of positive flows, and $C_1 \in R^{n_f \times n_p}$ is the connectivity matrix. The outlet flow matrix Q_o is defined as $\text{diag}\left(D_o C_1^T \hat{f} \right)$, where D_o in $R^{n_p \times n_p}$ is the decision matrix. D_o takes the value 1 for the outlet flow nodes and 0 for the other nodes. Similarly, the inlet flow matrix Q_i is given by $\text{diag}\left(D_i C_1^T \hat{f} \right)$, with D_i in $R^{n_p \times n_p}$ being the decision matrix, where D_i is 1 for the inlet flow nodes and 0 for the other nodes. The vector $H^* \in R^{n_p}$ represents the node hematocrit. Additionally, $\overline{H} \in R^{n_p}$ is the vector of inlet boundary conditions at time t. The boundary hematocrit is non-zero only at inlet nodes, where $\overline{H} = 0.35$.

The non-linear system of equations is solved iteratively by a fixed-point scheme[3] to obtain the flow, pressure, and hematocrit field h. First, flow and the pressure are calculated using Equation 10. Then the obtained flow values are used for calculating hematocrit in Equation 8. Figure 2. summarizes the iterative approaches for all

Step1. The bulk blood flow is first solved. (8)

Step2. The updated discharge hematocrit H_d is calculated using a convective matrix. (9)

Step3. Using Eq. 9, the discharge hematocrit update is reinserted into the bulk flow computation as a vascular resistance adjustment. (10)

Step4. The outer loop consists of an iterative bulk flow method that runs until the infinity norm of the difference between the old H_d, and the H_d-update reaches a tolerance threshold of 10^{-6}. (11)

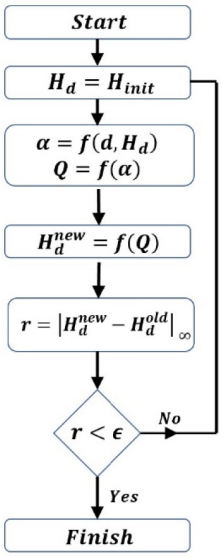

FIGURE 2 The flow chart describes the applied model's implementation to solve for the bulk blood flow, Q, and discharge hematocrit, H_d. The solution algorithm starts with the flow calculation, updating the diameter-hematocrit dependent resistance α with updated hematocrit, and iteration of the process until the difference between new H_d and old H_d reaches a tolerance threshold of 10^{-6}.

models in a flowchart to show the relationship between flow and hematocrit.

2.4 | Dynamic tracer-convection

The convection of a tracer obeys Equation 12. This species conservation balance states that accumulation equals net flux through the boundary of the balance envelope.

$$v_i \frac{dc_i}{dt} = -\oint c_i \mathbf{u}_i \cdot \mathbf{n}_i dS_i \tag{12}$$

Tracer concentrations are given by the vector concentration $c \in R^{n_p \times 1}$ for each balance envelope (point) at a time t. Let the components v_i of the vector $\mathbf{v} \in R^{n_p}$ denote the volume of the finite volume elements and set $V = \mathrm{diag}(\mathbf{v})$. The left-hand side tracer accumulation (Equation 12) in each volume can be discretized using implicit Euler methods as in Equation 17. Tracer flux at the inlet and outlet nodes are governed by the volumetric flows in their adjacent faces. The flux into an inlet node i adjacent to the face k is defined to be $f_k \underline{c}_i(t)$ where $\underline{c}(t) \in R^{n_p}$ is the time dependent vector of prescribed concentrations at the inlets (arterial input function). In other words, the components of the vector $\underline{c}(t)$ are nonzero only at the inlet nodes, at which points they take on prescribed time dependent boundary values. The flux out of an outlet node j adjacent to the face ℓ is defined to be $f_\ell c_j(t)$. In both cases we stay in accordance with the upwinding scheme by having the concentration at the boundary of a control volume equal that of the upwind node.

$$V \frac{d\mathbf{c}}{dt} = M_c \mathbf{c} + Q_o \mathbf{c} + Q_i \bar{\mathbf{c}} \tag{13}$$

Discretization of the convective flux. The convection matrix $M_c \in R^{n_p \times n_p}$ is given in (14)

$$M_c = -C_1^T [\![\mathrm{diag}(f)\, C_1]\!] = -C_1^T [\![FC_1]\!] = -C_1^T \max(FC_1, 0) \tag{14}$$

where $\boldsymbol{F} \in R^{n_f \times n_f}$ is the diagonal matrix whose diagonal entries are the elements of the flow vector $\boldsymbol{f}$, and the operator $[\![\cdot]\!]$ applies the operator $max(\cdot, 0)$ to each element of the input matrix. Here, $\boldsymbol{f} \in R^{n_f}$ denotes the vector of flows through the network faces in units of volume per unit time.

Boundary conditions. The in- and outflow boundary conditions are already included in the discretized formulation of (13). Thus its implementation is declarative without the need for logical statements. Then the flux matrices $Q_i \in R^{n_p \times n_p}$ and $Q_o \in R^{n_p \times n_p}$ are the inlet and outlet convection matrices defined by

$$Q_i = \mathrm{diag}(D_i C_1^T \boldsymbol{f}) \tag{15}$$

$$Q_o = \mathrm{diag}(D_o C_1^T \boldsymbol{f}) \tag{16}$$

Time integration. Time discretization can be done by the implicit Euler method as in (17). $\Delta t \in R$ denote the time step. The superscripts n and o denote the new and the old-time step respectively.

$$\frac{1}{\Delta t} V [\mathbf{c}^n - \mathbf{c}^o] = M_c \mathbf{c}^n + Q_o \mathbf{c}^n + Q_i \bar{\mathbf{c}}^n \tag{17}$$

Rearranging Equation 17 we obtain the recipe for computing $\mathbf{c}$ at the new time-step as the solution to a linear system.

$$[I - \Delta t V^{-1}(M_c + Q_o)]\mathbf{c}^n = \mathbf{c}^o + \Delta t V^{-1}(Q_i \bar{\mathbf{c}}^n) \tag{18}$$

TABLE 1 CBF perfusion range.

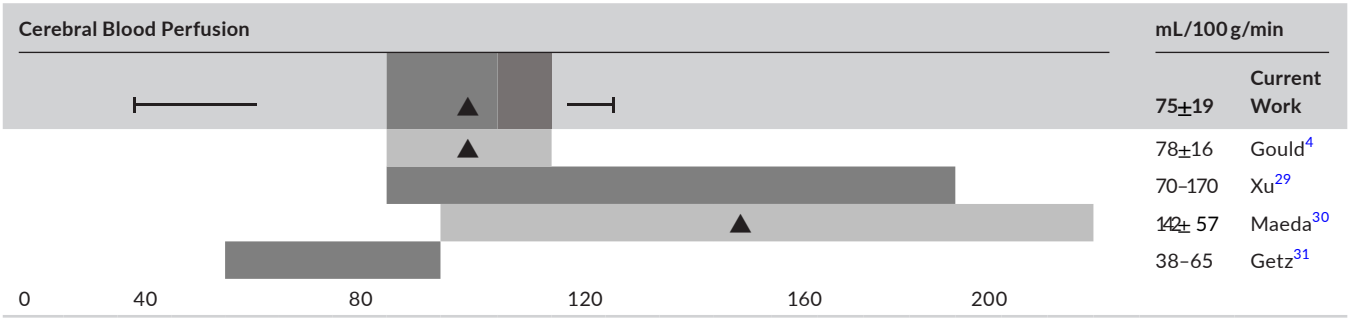

TABLE 2 Capillary RBC velocity range.

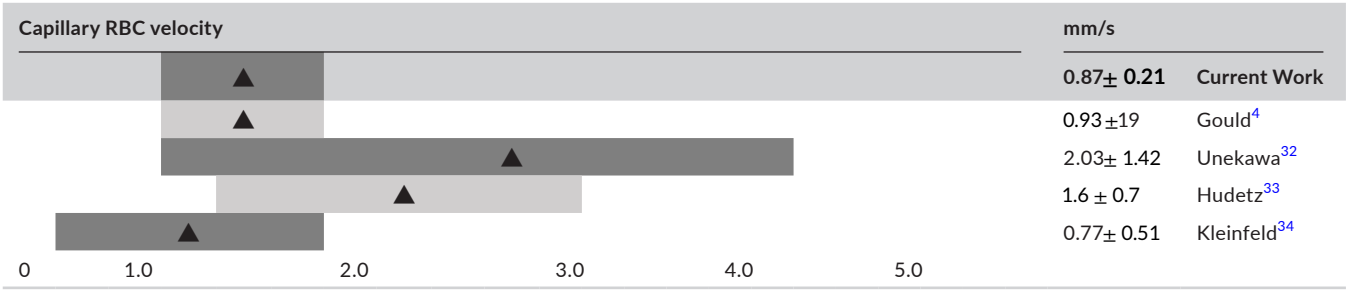

2.5 | Numerical verification

The mathematical model is validated against the flow parameters data in several blood networks for flow, pressure, and hematocrit. It is seen that the numerical solution is converged, and the residual value is small enough (less than 10^{-6}), and the mass and hematocrit continuity at the inlets and the network outlets are conserved. Blood perfusion and simulation of stalling events verifications are compared with the previous studies in the following sections.

Cerebral blood perfusion is measured as the rate of arterial blood supply to the volume of a tissue sample. Cerebral blood flow (CBF) is measured in milliliters of blood per one hundred grams of tissue per minute.[4] According to the definition, the CBF perfusion is the sum of flow rates of all arterial inlets over the voxel volume. Using the variable Ht viscosity model, the CBF was determined to be between 66 and 1.08 (ml/100 g/mL). In Tables 1 and 2, the cerebral blood perfusion and capillary RBC's velocity range of the current work, as well as the other reference, are compared; this demonstrates that the current work is within the range of past research studies and can be used as a validation criterion for the remaining simulations.

3 | RESULTS

3.1 | Structural properties

The modeling and analysis of blood flow in a complex network, including tortuous and random veins, is carried out using the two-photon microscopy mouse cortical microvascular blood network.[11] A network statistics analysis first obtained the morphological information about the mouse cortex, then used in the simulation. In Figure 3, several samples from the mouse cortex are extracted and visualized, in which arteries and veins are shown in red and blue, respectively. Extracted mouse brain sample is categorized into 18 layers to analyze the physiological properties of the network, including the number of vessels, resistance, and the length density, at each volume section of the network with 0.1 mm thickness from the surface to the depth of the blood network.

3.2 | Blood simulation

In the extracted sample cube network from the mouse cortex, blood enters the network from the thick pial arterial branches at the pial surface, traverses penetrating arteries and distributes into the network of capillaries and is collected in ascending veins which discharge into the pial veins. We performed path analysis to illustrate changes in blood flow patterns in the mouse cortical vasculature due to stalls. The CBF distribution in the mouse brain is studied along a sample path from the cortex in which blood enters the sample through the penetrating arteries from the pial surface of the mouse cortex and distribution through five capillaries in different depths of the network and collecting via the ascending veins and exit the blood network from the pial veins.

In Figure 4E, the hematocrit field is depicted for selected paths; the three longest penetrating arteries from the pial surface to the depth of the blood network, including the one that is shown with a dashed circle in Figure 4E, are chosen and indicated in Figure 4B–D, five pathways are shown in Figure 4A with their respective pressure field distributions. In order to emphasize the selected directed flow

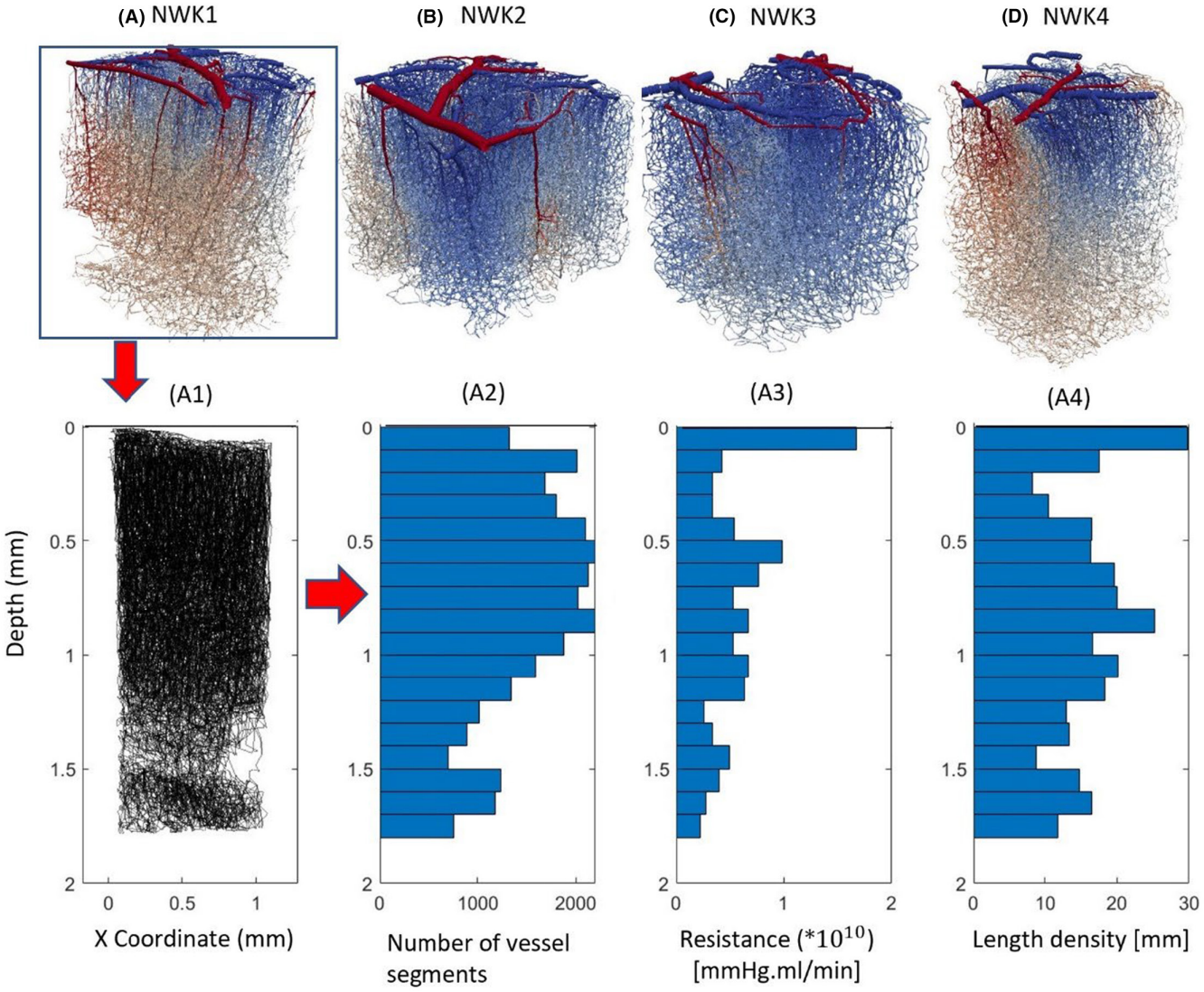

FIGURE 3 The mouse cortex microcirculatory sample networks (A–D). The colors correspond to pressure distribution in the blood network to distinguish the arteries and veins, where arteries are shown in red and veins are in blue. (A1). The visualization of the network (A1) in graph view consists of 39 547 vessels and 28 015 nodes. (A2) The number of vessels at each layer volume. (A3) The value of the resistance per layer volume. (A4) The value of the length density per volume, along with the network depth for 18 layers.

pathways, they were picked from the network following a simulation of blood flow and pressure. The entrance pressure is 120 mmHg, while the output pressure is 5 mmHg.[3,29,35] Flow analysis reflected that a perfusion pressure drop in the microcirculatory networks from 120 to 5 mmHg (15999–667 Pa) resulted in a mean tissue perfusion of 68.9 mL/100 g/min (11×10^{-6} m^3/kg/s) which is within experimentally observed ranges.[36,37]

Hematocrit is distributed unevenly from the main branch to the side branches of each bifurcation (Ht splitting rule), with the side branch with the larger diameter receiving more Ht than the other side branch. In Figure 4F–H, the dashed line represents the hematocrit splitting rule at bifurcations, exhibiting the ideal Ht split where Ht is divided evenly at each bifurcation. This shows that the bigger branches ("major branches") receive a greater proportion of the Ht split, as indicated by the red circles, while the thinnest branches receive a less proportion, as indicated by the blue circles.

In Figure 5, Ht distribution is displayed for all penetrating arteries demonstrating that the value of Ht increases from the pial surface to the depth of penetrating arteries. A 3D display (inlay) illustrates the variation in Ht along the penetrating arteries. The Ht distribution along all penetrating arteries originates from the pial surface downwards into the blood network using the cuboid sample from the mouse brain cortex. The Ht along the penetrating arteries increases in accordance with the Ht splitting rule. This phenomenon could be captured using the kinematic plasma skimming model (KPSM) applied in this study.[4]

3.3 | Occlusion simulation

Capillaries play an important role in the oxygen and nutrient delivery to the tissues. Capillaries have diameters around 5–10 μm

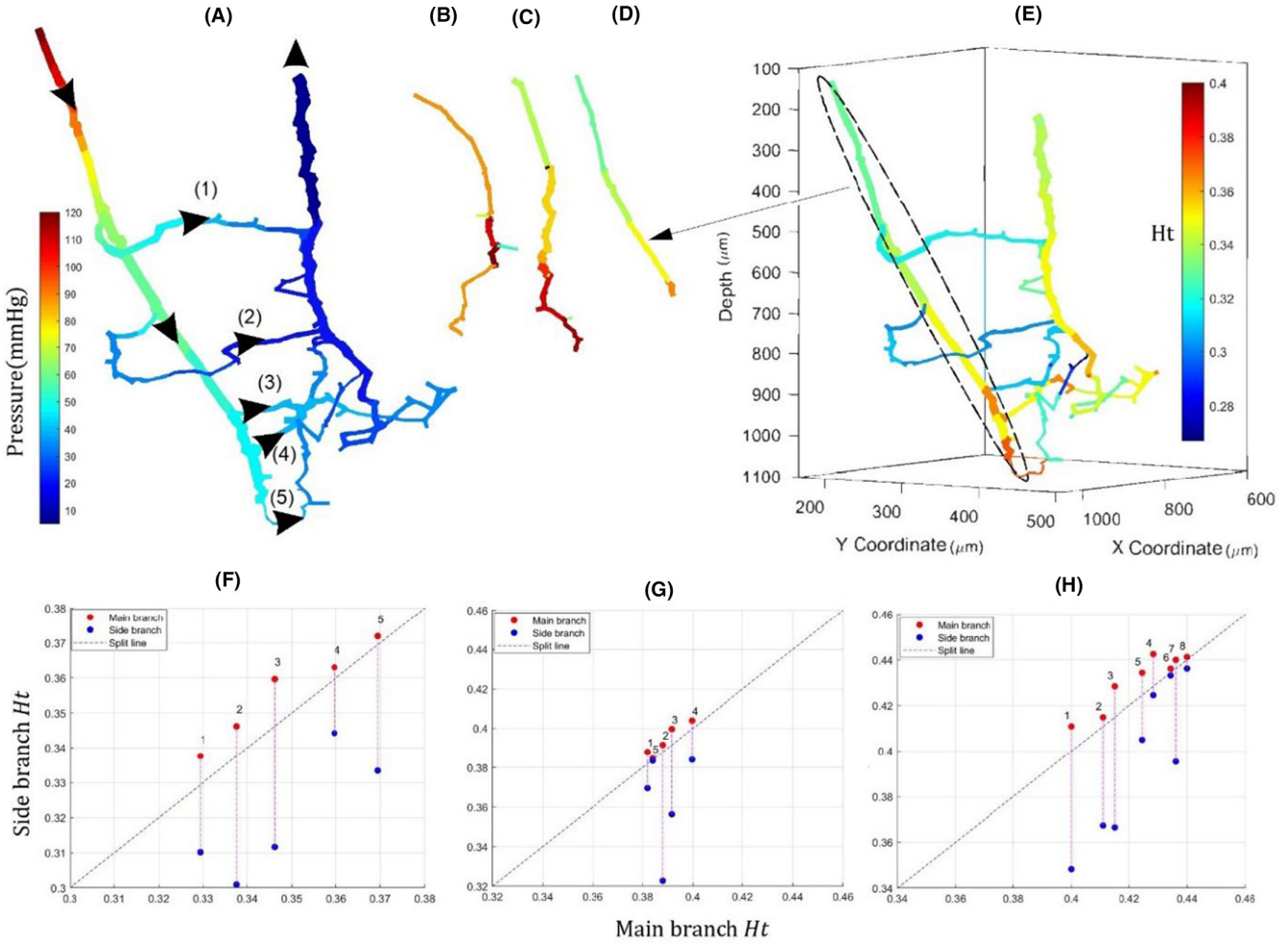

FIGURE 4 The simulation result for the flow-directed paths from the mouse brain cortex. (A). Pressure (mmHg) distribution on five selected paths, including all bifurcations along penetrating arteries, capillaries, and ascending veins (B-D). Ht distribution along the main penetrating arteries 1–3, (E) Entire paths Ht with indicating the location of the penetrating artery 1. Ht is split in bifurcations along the three longest penetrating arteries; The side branch is shown in the blue circle, the main branch (main) is in the red circle, and the dashed line represents the Ht ideal distribution at (F). Penetrating artery 1, (G). Penetrating artery 2, and (H). Penetrating artery 3, where the vertical and horizontal axis shows the sides and main Ht, respectively.

which makes them vulnerable to occlusion. Capillary occlusion can lead to reduced blood flow to the surrounding tissues, which can result in ischemia and consequently to tissue damage.[16] Microstrokes are thought to occur primarily at the capillary level.[13] Capillaries have a high surface area-to-volume ratio, which makes them susceptible to occlusion induced changes in blood flow and pressure. Capillaries also lack the smooth muscle cells found in larger vessels, which limits their ability to regulate blood flow and respond to changes in vascular tone.[38] In our simulation study, mouse brain sample cortex blood network (NWK1) was used for studying the effect of capillary stalls.

We performed blood flow, pressure, and Ht simulations on the healthy network (considered a zero-stalled scenario) and on the occluded network with various degrees of occlusions to determine the effect of capillary stalls on hemodynamic parameters. For this study, occlusions were implemented by selecting up to 20% of vessels at random from the capillary ensemble. The relatively high range of 20% stalls was chosen as in a previous study.[10] To model capillary stalls, the flow resistance in the stalled segments was increased by a factor of 1000 compared to baseline resistance.

Figure 6 summarizes simulation results visualizing the occlusion effects on Ht distribution, cerebral blood flow, and rerouted flows in the blood network in 3D view. Figure 6A presents the blood pressure field in the healthy blood network tracing blood from the pial surface through the penetrating arteries, the capillary bed and finally leaving the network through the pial veins. As expected, blood flow is reduced with increasing degree of stalls as shown in Figure 6C which summarizes the change in blood flow caused by stalling of capillaries, the color map from blue to red shows the percentage of the flow change in comparison to the healthy network.

In addition to increases in resistance, substantial network effects were observed. Figure 6B shows flow reversal in large portions of the network in red. The large number of segments with

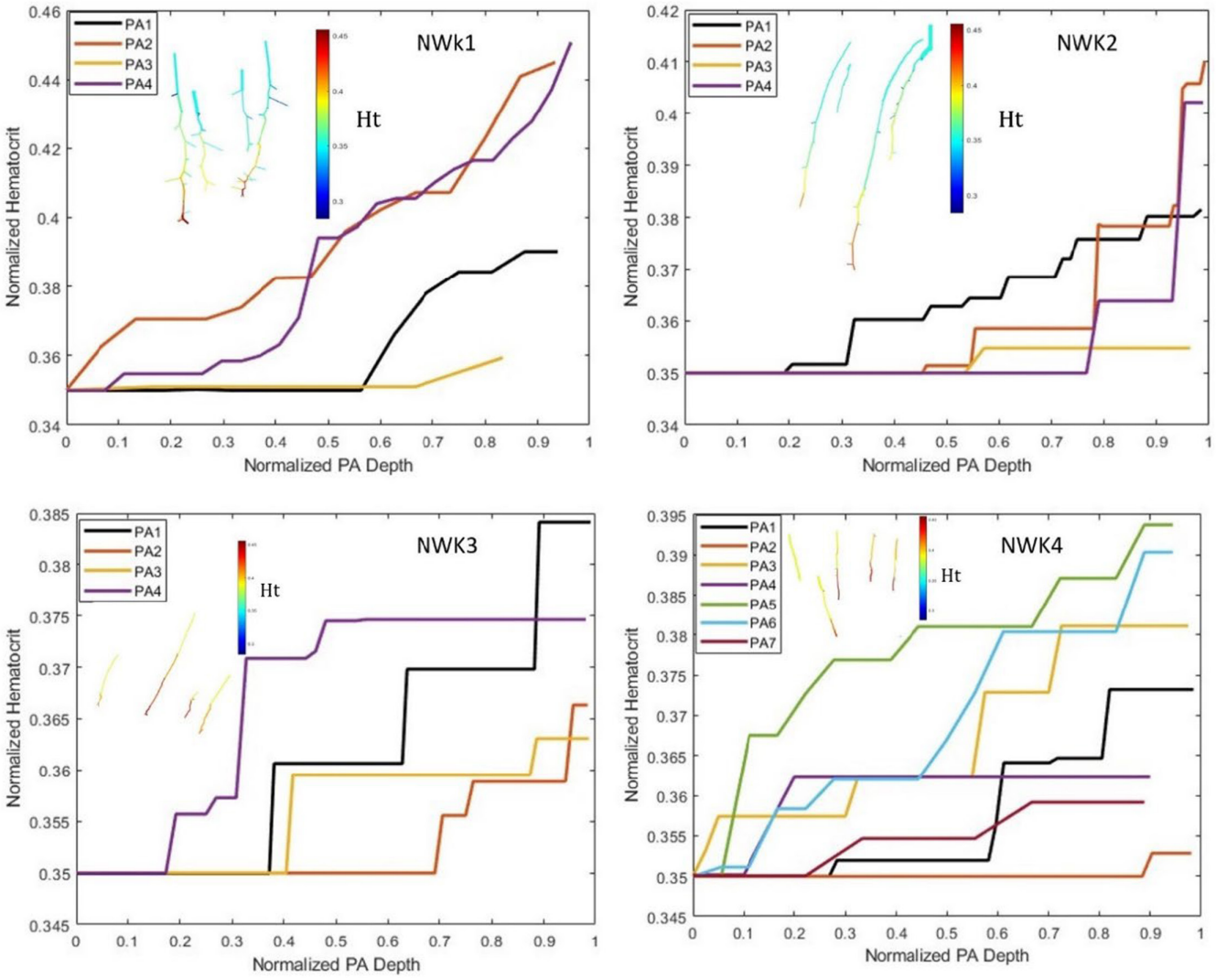

FIGURE 5 The hematocrit (Ht) increases along the penetrating arteries from the pial surface towards the depth of the network using four different mouse brain cortex samples. The plotted Ht for all penetrating arteries. Alongside the 3D visualization of the penetrating arteries and their position in the blood network.

changes in flow direction are indicative of blood flow redistribution and rerouting in the capillary bed, in effect following alternative paths that bypass the occluded vessels to convey blood past the obstruction.

The Ht simulation presented in Figure 6D shows that Ht change occurs mainly in vessels located in deeper in the cortical mantle.

We also tracked the effect of stalls on flow paths in the network and hematocrit variation in neighboring paths. Five typical paths from the inlet to outlet, each with a different depth from the pial surface, are selected for illustrating typical trends. Each path has numerous side branches and only the routes that include the vessels that direct blood from the inlet to the outlet of the network are selected and visualized. After the occlusion of each path, the effect of the Ht change on the other paths in the network is visualized in Figure 7. The red and gray vessels show Ht reduction or increase after the occlusion, respectively. The Ht variation with increasing and decreasing RBC flux densities in each path result from vessel occlusion as depicted in Figure 7A–E.

The variation of the Ht at each path is depicted in Figure 7F (paths are also shown in Figure 6A). The bar plot shows the proportion of vessels that encountered the increase and decrease in Ht along each path, shown in blue and red, respectively.

3.4 | Effect of stalls on micro circular network integrity and tracer transit

We compared flow changes due to stalls to connected component analysis (CCA) presented previously.[39] Connectivity component analysis allows to ascertain the extent to which occlusion impairs network connectivity and cortical blood perfusion. Two experiments were undertaken: the first involved randomly stalling all

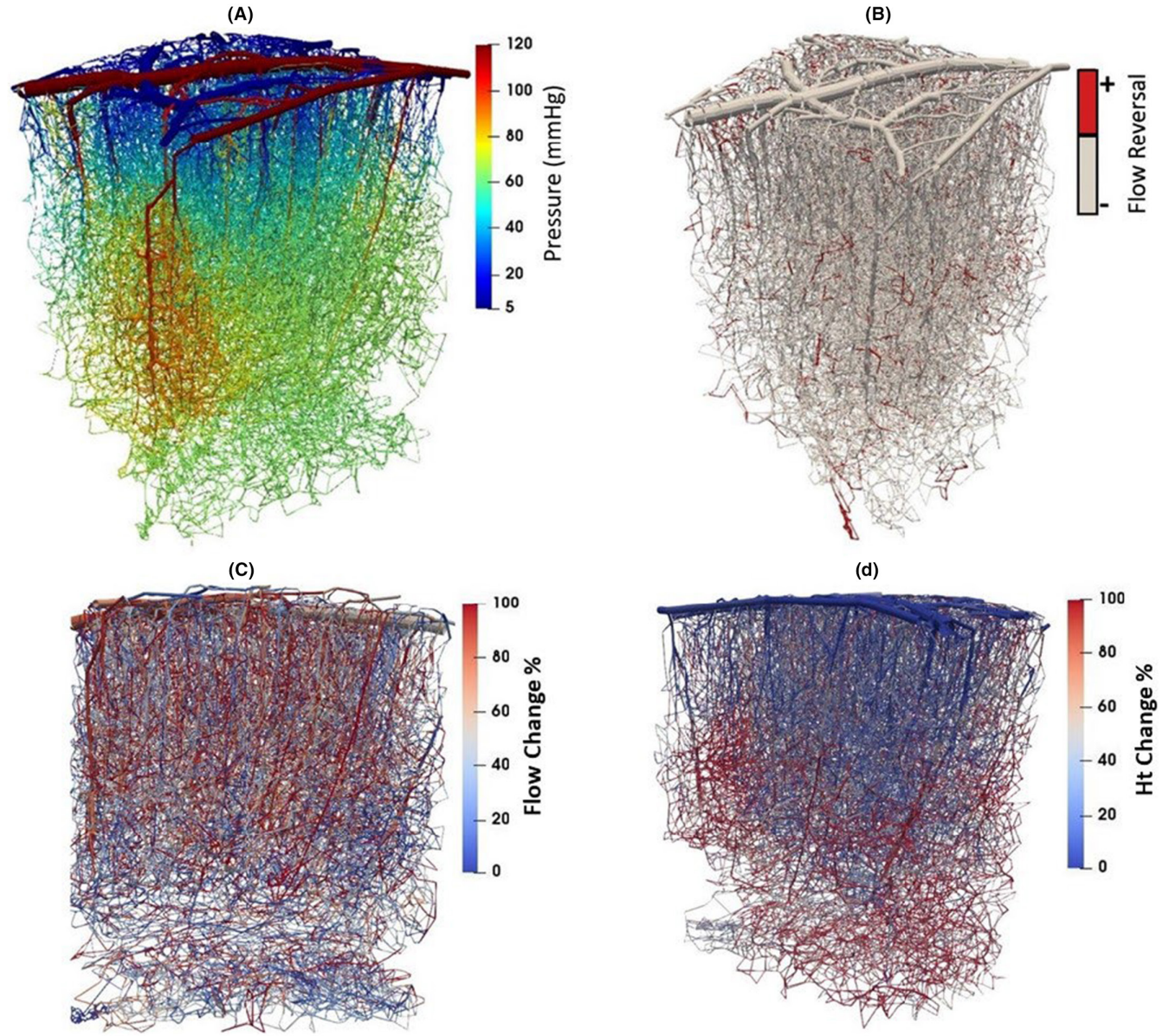

FIGURE 6 The 3D images of a portion of the mouse cerebral vasculature, comprising pial arteries, penetrating arteries, capillaries, and ascending and pial veins based on numerical simulations. (A). Pressure field in the healthy blood network (mmHg) (B). Flow reversal in the blood network, shown in red, vessels with no flow reversal are depicted in gray for a 20 percent occlusion; (rerouting occurs at red vessels) (C). Flow changes percentage in all network vessels following a 20 percent network occlusion compared to a healthy network (D). Ht change in percentage following the occlusion of 20 percent of capillary vessels.

vessels up to 20%, while the second specifically focused on capillary stall. Our results reproduce findings by Kleinfeld,[39] according to which occlusion in fraction of 0.425 led to a complete disconnection of the network.

Flow reduction due to stalls was more severely affected than that suggested by the CCA. Total flow changes (=total fluxes from inlets to outlets) for different occlusion levels are depicted in Figure 8. Moreover, the trends in flow decrease were found to become gradually more nonlinear probably due to the nonlinearity in the viscosity law. The blood flow decreases steadily beyond 2 percent occlusion. Insufficient perfusion leading to eventual circulation failure in the network seems to occur beyond 10 percent occlusion; this phenomenon can also be seen in the tracer convection simulation by the increase of the tracer concentration in the network.

Tracer transit simulations. Tracer convection simulations were carried out using the relations in Equation (12) of section 2.3 to capture the effect of stalling on transport phenomena. With increasing occlusion levels, flow decreased as expected because stalls augment overall resistance to flow. Further results listed in Appendix B further suggest that mean transit times for the whole voxel signal shifted, but a clear trend could not be established in

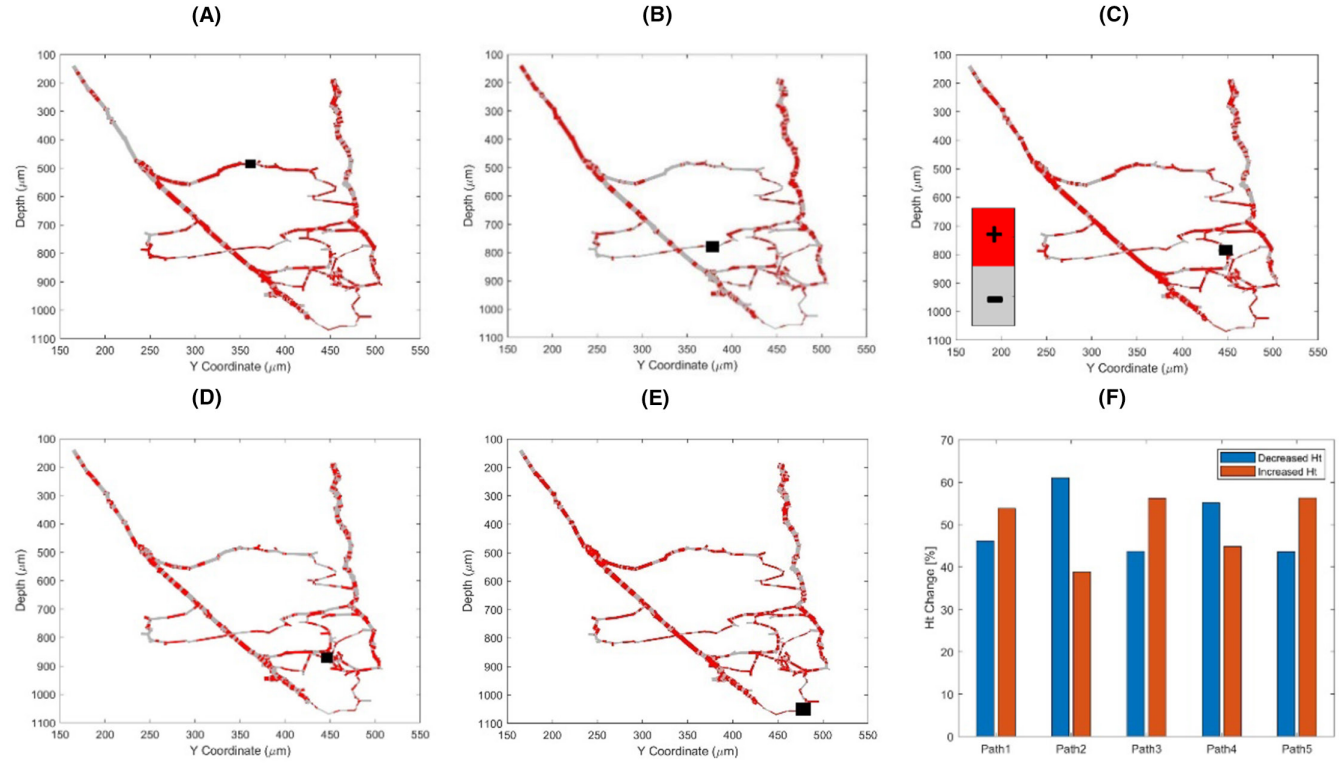

FIGURE 7 Variations in hematocrit (Ht) correspond to the occluded vessels shown by the small black square at each path. (A-E). Variation of Ht at each occluded vessel neighbors, Ht increase (+) and decrease (−) shown in red, and gray, respectively. (F). The statistical variation of the Ht along each path after occlusion and the percentage amount of the Ht vessels increase and decrease after occlusion, where the paths are shown in Figure 6A.

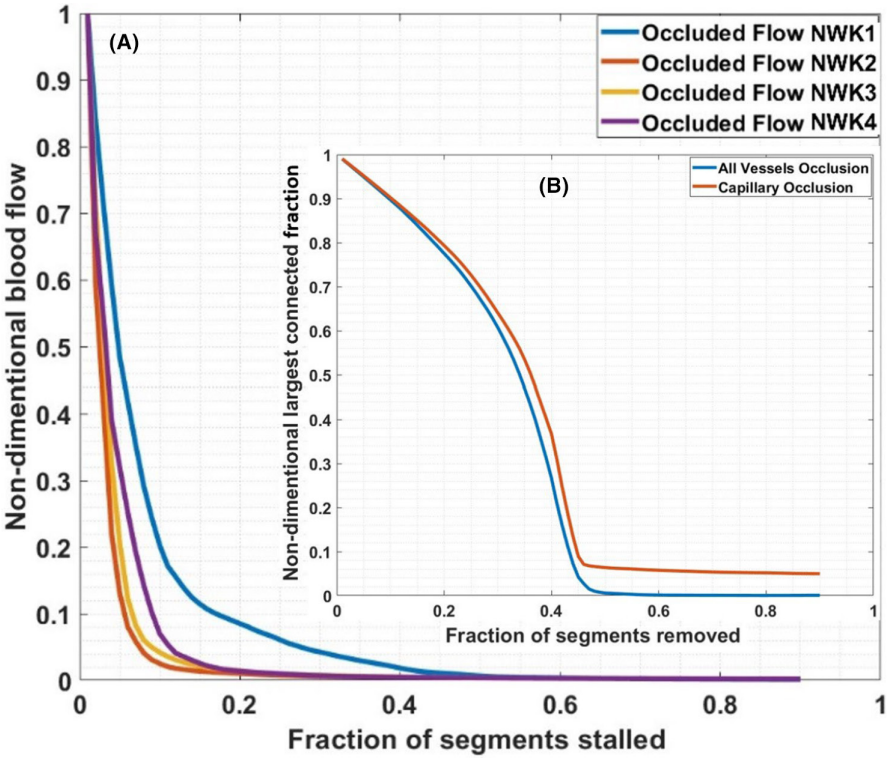

FIGURE 8 Simulation of stalling effect on cerebral blood flow and analysis of connected components. (A). Inlet blood flow reduction for different levels of occlusions. (B). The blood network's largest component connection for varying occlusion ratios [occlusion limited to the capillary bed (orange profile); stalls for all vessels (blue profile)].

the preliminary analysis. This subtle response might be due to the combined effect of lower flow with concomitant reduction in the intravascular volume accessible to flow. Thus, two competing influences of blood volume (CBV) and blood flow (CBF) have their effect on transit time. We also observed a slight increase in mean hematocrit distribution.

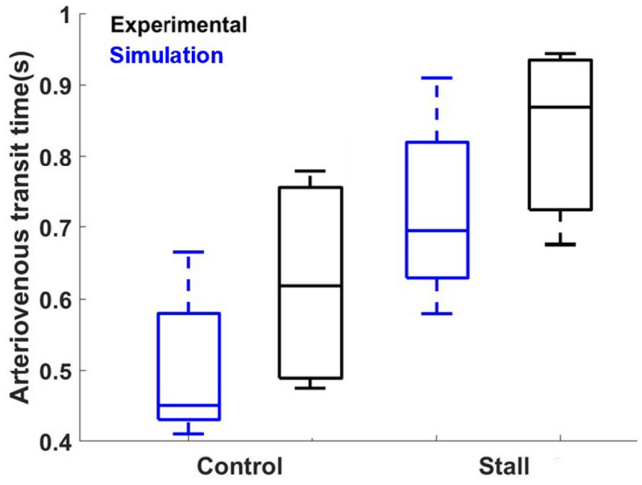

FIGURE 9 Quantification of the duration required for blood to traverse the arteriovenous network. The arteriovenous transit time in the current work before (control) and after stall simulation up to 10% stall and, experimental study up to 8% stall, the stall group shows a notably longer average arteriovenous transit time in comparison to the control group.[40]

3.5 | In-vivo validation of transit time shifts after microvascular stall

To support our predictions, a preliminary experimental validation of micro stalls is reported here comparing mice (control) with specimen treated with LPS challenge (LPS mice) which causes systemic inflammation group. In brief, the impact of intraperitoneal lipopolysaccharide (LPS) injection-induced systemic inflammation on cerebral vasculature and microcirculation in mice was examined by investigating shifts in the transit time from pial arteries to pial veins. Experimental measurements of transit times in both pial arteries and pial veins are graphically represented in Figure 9. The data show an increase in arteriovenous transit time in arteries and veins in the stall group compared to the control group.

In our simulations for control mice, the in vivo measured transit time differences were determined to be 0.45 ± 0.1 s. Notably, in the stall mouse cohort, this value exhibited an increase to 0.69 ± 0.12 s, as quantified and illustrated in Figure 9, which presents the arteriovenous transit time for both the simulations and the experiment. Our simulation results show that stalls increased arterial to venous transit time, a trend that was matched in stall mouse experiments which experiences a significant increment when compared to the control group.[40]

4 | DISCUSSION

This paper investigates the impact of capillary stalls on hemodynamics properties including the flow, pressure, hematocrit, transit time, and tracer convection for the mouse cortex samples.

Single vessel stalls induce no significant perfusion deficits owing to redundancy in the capillary network and its capacity to redirect blood flow in response to minor obstructions. However, mechanistic simulations indicate that elevated stall levels (more than 2% stalled capillaries) may impair perfusion of the entire network, when no compensatory mechanisms are in place, which were not accounted for in our simulations. Stalling vessels well below a fraction of 0.425 of the whole capillaries led to the collapse of the blood flow in all network simulations blood flow in the network stopped completely at much lower levels than suggested by percolation limit (approximately 0.425 stalled vessel fraction).

We reported that stalling also induces substantial network effects of rerouted capillary flow directions. Capillary stalls cause flow reversals in a significant portion of the capillary network. The ability to reroute flows to alternative paths around occluded vessels available in a healthy brain may decrease with age. Consequently, it is essential to further analyze the redirected channels to determine the probability of blood flow path replacement due to blockage.

In addition to rerouted flows, stalling altered Ht distribution. Normally, Ht is higher in the main branch of the penetrating arterioles with smaller Ht levels inside branches. We further quantified the Ht distribution changes with path analysis by tracking flow from the penetrating artery (PA) along different capillary depths leading to ascending vein (AV). We found that Ht levels increased in penetrating arteries downwards into the depth of the blood network.[3] The redirection of the blood flow also induces Ht shifts (increase and decrease) at the upstream and downstream of the occluded vessels. Simulations showed a higher mean in Ht levels and higher heterogeneity of RBC distribution. The results indicate that Ht changes occur at the small vessels at the capillary level.

To test whether stall can be detected by in vivo fluorescence imaging we performed simulated transit time of tracer perfusion experiments. In virtual tracer infusion simulations, we recorded difference in time-to-peak in pial arteries and in pial veins. We detected an increase of 0.24 s from 0.45 ± 0.1 s in the control group to 0.69 ± 0.12 s in the stalled mouse cohort. The predictions matched our preliminary experimental evaluation of transit time shifts in both pial arteries and pial veins (control: 0.62 ± 0.11, stall: 0.84 ± 0.09). The agreement of results from both simulation and experimentation underscores the possibility of detecting stalls with in vivo transit time measurements. Such metric would be an important biomarker for the presence of capillary stalls.

4.1 | Perspectives

Analyzing cerebral microvasculature's role in cognitive dysfunction, this study explores the impact of capillary stalls on microcirculatory characteristics in the mouse cortex. Using a deterministic mathematical model, parameters like pressure, flow, transit time, and hematocrit are assessed during stalling events. These findings, indicating changes in blood dynamics, may have implications for Alzheimer's disease development, highlighting the importance of understanding microcirculatory influences on cognitive health.

AUTHOR CONTRIBUTIONS

Mohammad Jamshidi (Data Analysis, Software, Imaging, and Composition). Thomas Ventimiglia (Theory, Software, and Composition). Patrice Sudres (Data Analysis and Composition). Cong Zhang (Experimental, Data Analysis). Frédéric Lesage (Experimental, Conceptualization, Supervision, and composition). William Rooney (Conceptualization, Supervision, and Composition). Daniel Schwartz (Imaging and Composition). Andreas A Linninger (Conceptualization, Theory, Software, Supervision, and Composition).

ACKNOWLEDGMENTS

This work was supported in part by the NIH National Institute of Health, Neurological Disorders and Stroke (https://www.ninds.nih.gov/) under Grant number NIH NINDS 1R21NS099896. And the National Institute of Health, National Institute of Aging (https://www.nia.nih.gov/) under grant NIH NIA1R56AG066634-01 and NIH NINDS U19NS123717.

FUNDING INFORMATION

NIH National Institute of Health, Neurological Disorders and Stroke (https://www.ninds.nih.gov/) under Grant number NIH NINDS 1R21NS099896. National Institute of Health, National Institute of Aging (https://www.nia.nih.gov/) under grant NIH NIA1R56AG066634-01 and NIH NINDS U19NS123717.

DATA AVAILABILITY STATEMENT

The collaborative laboratories (co-authors) supplied the experimental source data for this study. Access to the experimental source data is available through the references provided in the Methods section and open-source public repositories. Samples of synthetic network data are available at https://github.com/LPPDAdmin

ORCID

Frédéric Lesage https://orcid.org/0000-0003-3699-1283

REFERENCES

1. Yang R, Wang A, Ma L, et al. Hematocrit and the incidence of stroke: a prospective, population-based cohort study. *The Clin Risk Manag*. 2018;14:2081-2088.
2. Chen SH, Bu XL, Jin WS, et al. Altered peripheral profile of blood cells in Alzheimer disease: a hospital-based case-control study. *Medicine (Baltimore)*. 2017;96(21):e6843.
3. Hartung G, Vesel C, Morley R, et al. Simulations of blood as a suspension predict a depth-dependent hematocrit in the circulation throughout the cerebral cortex. *PLoS Comput Biol*. 2018;14(11):e1006549.
4. Gould IG, Tsai P, Kleinfeld D, Linninger A. The capillary bed offers the largest hemodynamic resistance to the cortical blood supply. *J Cereb Blood Flow Metab*. 2017;37(1):52-68.
5. Damseh R, Yuankang L, Xuecong L, et al. A simulation study investigating potential diffusion-based MRI signatures of microstrokes. *Sci Rep*. 2021;11(1):1-15.
6. Kochanek KD, Xu J, Murphy SL, Tejada-Vera B. *"Deaths: Final Data for 2014." National Vital Statistics Reports: from the Centers for Disease Control and Prevention*. Vol 65. National Center for Health Statistics, National Vital Statistics System; 2016:1-122.
7. Matthews KA, Xu W, Gaglioti AH, et al. Racial and ethnic estimates of Alzheimer's disease and related dementias in the United States (2015-2060) in adults aged ≥65 years. *Alzheimers Dement*. 2019;15(1):17-24.
8. Tejada-Vera B. Mortality from Alzheimer's disease in the United States: data for 2000 and 2010. *NCHS*. 2013;(116):1-8.
9. Hartung G, Badr S, Moeini M, et al. Voxelized simulation of cerebral oxygen perfusion elucidates hypoxia in aged mouse cortex. *PLoS Comput Biol*. 2021;17(1):1008584.
10. Cruz Hernández JC, Bracko O, Kersbergen CJ, et al. Neutrophil adhesion in brain capillaries reduces cortical blood flow and impairs memory function in Alzheimer's disease mouse models. *Nat Neurosci*. 2019;22:413-420.
11. Blinder P, Tsai PS, Kaufhold JP, Knutsen PM, Suhl H, Kleinfeld D. 2013. The cortical angiome: an interconnected vascular network with noncolumnar patterns of blood flow. *Nat Neurosci*. 2013;16:889-897.
12. Nishimura N, Schaffer CB, Friedman B, Lyden PD, Kleinfeld D. Penetrating arterioles are a bottleneck in the perfusion of neocortex. *PNAS*. 2007;104:365-370.
13. Schmid F, Conti G, Jenny P, Weber B. The severity of microstrokes depends on local vascular topology and baseline perfusion. *elife*; 2021;10:e60208.
14. El Amki M, Glück C, Binder N, et al. Neutrophils obstructing brain capillaries are a major cause of No-reflow in ischemic stroke. *Cell Rep*. 2020;33:108260.
15. Erdener SE, Tang J, Kiliç K, et al. Dynamic capillary stalls in reperfused ischemic penumbra contribute to injury: a hyperacute role for neutrophils in persistent traffic jams. *J Cereb Blood Flow Metab*. 2021;41:236-252.
16. Menger MD, Jaeger S, Walter P, Hammersen F. Microvascular ischemia-reperfusion injury in striated muscle: significance of "no-reflow" phenomenon. *J Surg Res*. 1992;52(4):387-393. doi:10.1016/0022-4804(92)90169-p
17. Metea MR, Newman EA. Glial cells dilate and constrict blood vessels: a mechanism of neurovascular coupling. *J Neurosci*. 2006;26(11):2862-2870. doi:10.1523/JNEUROSCI
18. Iadecola C. The neurovascular unit coming of age: a journey through neurovascular coupling in health and disease. *Neuron*. 2017;96(1):17-42. doi:10.1016/j.neuron.2017.07.030
19. Liu X, Wang S, Yi M, et al. Neurovascular coupling: structure and function in health and disease. *Front Physiol*. 2019;10:1082. doi:10.3389/fphys
20. Cheng JY, Shih YI, Chen YT, et al. A computational model of cerebral oxygen transport and metabolism under hypoxia and hyperoxia. *Med Eng Phys*. 2019;72:36-44. doi:10.1016/j.medengphy
21. Kiani MF, Cutaia MV. Modeling and simulation of blood flow and oxygen transport in the microcirculation. *Crit Rev Biomed Eng*. 2011;39(3):235-261.
22. Mantegazza A, Clavica F, Obrist D. In vitro investigations of red blood cell phase separation in a complex microchannel network. *Biomicrofluidics*. 2020;14(1):014101.
23. Billett HH. Hemoglobin and hematocrit. In: Walker HK, Hall WD, Hurst JW, eds. *Clinical Methods: the History, Physical, and Laboratory Examinations*. 3rd ed. Butterworths; 1990. https://www.ncbi.nlm.nih.gov/books/NBK259/
24. Gould IG, Linninger AA. Hematocrit distribution and tissue oxygenation in large microcirculatory networks. *Microcirculation*. 2015;22(1):1-18.
25. Lipowsky HH, Usami S, Chien S. In vivo measurements of "apparent viscosity" and microvessel hematocrit in the mesentery of the cat. *Microvasc Res*. 1980;19(3):297-319.
26. Pries AR, Secomb TW, Gessner T, Sperandio MB, Gross JF, Gaehtgens P. Resistance to blood flow in microvessels in vivo. *Circ Res*. 1994;75(5):904-915.

27. Pries AR, Secomb TW, Gaehtgens P. Biophysical aspects of blood flow in the microvasculature. *Cardiovasc Res*. 1996;32(4):654-667.
28. Park CS, Hartung G, Alaraj A, Xinjian D, Charbel FT, Linninger AA. Quantification of blood flow patterns in the cerebral arterial circulation of individual (human) subjects. *International Journal for Numerical Methods in Biomedical Engineering*. 2020;36:e3288.
29. Xu K, Radhakrishnan K, Serhal A, et al. In: LaManna JC, ed. *Oxygen Transport to Tissue XXXII*. Springer ScienceþBusiness Media; 2011.
30. Maeda K, Mies G, Olah L, et al. Quantitative measurement of local cerebral blood flow in the anesthetized mouse using intraperitoneal [C-14] iodoantipyrine injection and final arterial heart blood sampling. *J CerebBlood Flow Metab*. 2000;20:10-14.
31. Gertz K, Priller J, Kronenberg G, et al. Physical activity improves long-term stroke outcome via endothelial nitric oxide synthase-dependent augmentation of neovascularization and cerebral blood flow. *Circ Res*. 2006;99:1132-1140.
32. Unekawa M, Tomita M, Tomita Y, Toriumi H, Miyaki K, Suzuki N. RBC velocities in single capillaries of mouse and rat brains are the same, despite a 10-fold difference in body size. *Brain Res*. 2010;1320:69-73.
33. Hudetz AG, Feher G, Kampine JP. Heterogeneous autoregulation of cerebrocortical capillary flow: evidence for functional thoroughfare channels? *Microvasc Res*. 1996;51:131-136.
34. Kleinfeld D, Mitra PP, Helmchen F, Denk W. Fluctuations and stimulus-induced changes in blood flow observed in individual capillaries in layers 2 through 4 of rat neocortex. *Proc Natl Acad Sci U S A*. 1998;95:15741-15746.
35. Hartung G, Alaraj A, Linninger A. Chapter 21– walk-in brain: virtual reality environment for immersive exploration and simulation of brain metabolism and function. In: Martín M, Eden MR, Chemmangattuvalappil NG, eds. *Computer Aided Chemical Engineering*. Vol 39. Elsevier; 2016:649-658. (Tools For Chemical Product Design).
36. Peyrounette M, Davit Y, Quintard M, Lorthois S. Multiscale modelling of blood flow in cerebral microcirculation: details at capillary scale control accuracy at the level of the cortex. *PLoS One*. 2018;13(1):e0189474.
37. El-Bouri WK, Payne SJ. Multi-scale homogenization of blood flow in 3-dimensional human cerebral microvascular networks. *J Theor Biol*. 2015;380:40-47.
38. Mchedlishvili G. Microcirculation of the brain. *Handbook of Physiology, the Cardiovascular System*. Vol IV. American Physiological Society; 1982:773-800.
39. Ji X, Ferreira T, Friedman B, et al. Brain microvasculature has a common topology with local differences in geometry that match metabolic load. *Neuron*. 2021;109(7):1168-1187.
40. Zhang C, Delafontaine-Martel P, Jamshidi M, Linninger A, Lesage F. Evaluation of cerebral microcirculation in a mouse model of systemic inflammation. *Neurophotonics*. 2024;61:1-10.

How to cite this article: Jamshidi M, Ventimiglia T, Sudres P, et al. Impact of stalling events on microcirculatory hemodynamics in the aged brain. *Microcirculation*. 2024;00:e12845. doi:10.1111/micc.12845

APPENDIX A

See Table A1.

TABLE A1 Table of variables for Pries's in vitro viscosity models.[26,27]

Symbol	Definition	Units	Value
μ_{vM}	Apparent viscosity Modified	cP	F(dia, H_d)
μ_{vitro}	Apparent viscosity Original	cP	F(dia, H_d)
D	Vessel diameter	μm	Known scalar
H_d	Discharge hematocrit	Vol%	Unknown scalar
μ_{45}	Viscosity at H_d =0.45	cP	F(dia, H_d)
μ_{plasma}	Plasma viscosity	cP	1.0

APPENDIX B

$$\mu_{vM} = \left[1 + (\mu^*_{0.45} - 1)\frac{(1-H_d)^C - 1}{(1-0.45)^C - 1}\left(\frac{D}{D-1.1}\right)^2\right]\left(\frac{D}{D-1.1}\right)^2 \mu_{plasma} \quad \text{(A-1)}$$

$$\mu^*_{0.45} = 6\,e^{-0.085\,D} + 3.2 - 2.44e^{-0.06D^{0.645}} \quad \text{(A-2)}$$

$$C = (0.8 + e^{-0.075\,D})\left(-1 + \frac{1}{1 + 10^{-11}D^{12}}\right) + \frac{1}{1 + 10^{-11}D^{12}} \quad \text{(A-3)}$$

B. | TRANSIT TIME SHIFTS IN TRACER CONVECTION SIMULATION

Tracer convection simulations were carried out using the relations in Equation (20) of section 2.3 to capture the effect of stalling on the transport phenomena; the tracer is injected into the blood network from the inlet pial arteries by using an arterial input function (AIF) equal to a Dirac delta function. The outlet concentration curve then approximates the impulse response function $h(t)$ of the entire network. The mean transit time (MTT) and transit time heterogeneity (TTH) in Table 4 are thus computed as the first and second moments of $h(t)$.

TABLE A2 The mean and the standard deviation of hematocrit (Ht), mean transit time (MTT), and blood flow.

		No-Occlusion	1%	2%	5%	10%	20%
Ht	μ	0.356	0.356	0.356	0.358	0.359	0.364
	σ	0.052	0.049	0.048	0.054	0.051	0.057
$h(t)$	MTT [s]	1.74	1.77	1.75	1.72	1.68	1.44
	TTH $[s^2]$	8.84	10.60	9.18	9.94	9.43	4.33
Flow $[\mu m^3/s]$	μ	37644.8	37462.9	37272.0	36511.9	35658.2	32891.3
	σ	263448.7	262465.9	261483.7	257252.6	251694.9	233991.4

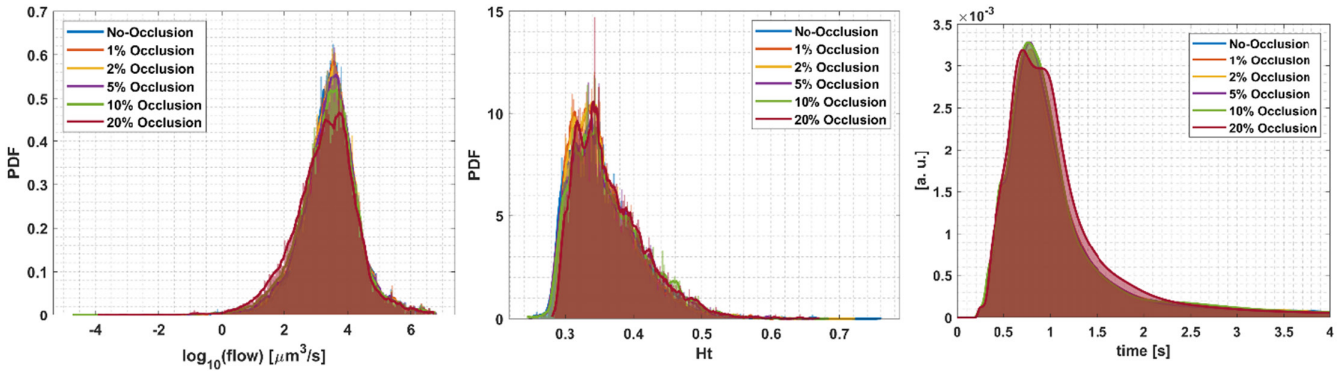

FIGURE A1 (A) A semilog plot of the probability density functions of the flow in the network for different occlusion percentages, (B) the probability density functions of Ht, (C) the impulse response functions which form the basis of the transit time analysis in Table 4.

In Figure 10A,B, a statistical analysis was conducted for the flow and Ht, associated with the occluded network. Flows through vessels tend to decrease with severity of occlusions as in Figure 10A. There is also an increase in the mean of Ht distribution shown in Figure 10B. Moreover, Figure 10C. shows the impulse response function, $h(t)$ for different levels of stalling. The means and variances of flow and Ht are collected in Table 4.

$$\mathrm{MTT} = \frac{\int_0^\infty t \cdot h(t)\, dt}{\int_0^\infty h(t)\, dt} \tag{B-1}$$

$$\mathrm{TTH} = \frac{\int_0^\infty (t - \mathrm{MTT})^2 \cdot h(t)\, dt}{\int_0^\infty h(t)\, dt} \tag{B-2}$$